Article:

Adamu, M orcid.org/0000-0002-5028-9370, Jacob, KT and Kale, GM orcid.org/0000-0002-3021-5905 (2020) Assessment of MgZr4P6O24 as a Solid Electrolyte for Sensing Mg in Molten Non-Ferrous Alloys. Journal of the Electrochemical Society, 167 (2). 027532. ISSN 0013-4651

https://doi.org/10.1149/1945-7111/ab6556

Assessment of $MgZr_4P_6O_{24}$ as a Solid Electrolyte for Sensing Mg in Molten Non-Ferrous Alloys

Mohammed Adamu[1], K.T Jacob[2] and Girish M. Kale[1*]

[1]School of Chemical and Process Engineering, University of Leeds, Leeds LS2 9JT, United Kingdom

[2]Department of Materials Engineering, Indian Institute of Science, Bengaluru 560012, India

---

The potential solid electrolyte, $MgZr_4P_6O_{24}$ was prepared using a modified sol-gel method. Both structural and electrical properties of the solid electrolyte were determined. DSC-TGA analysis indicated that pure dried xerogel when calcined at 900°C converts to single phase $MgZr_4P_6O_{24}$ nanopowder with good crystallinity. Pellets of 13mm diameter and 3.8mm thickness made by uniaxial compression were sintered at 1300°C for 24h. XRD and HR-TEM indicated that the crystalline phase is monoclinic having crystallite size of approximately 40nm. The sintered pellets were stable in the temperature range from 1000 to 1300°C, with minor extraneous peaks indicating traces of a coexistent second phase ($Zr_2P_2O_9$) at the higher temperature. Using impedance spectroscopy, the electrical conductivity of $MgZr_4P_6O_{24}$ was determined as 7.23×10^{-3} Scm^{-1} at 725°C. $MgZr_4P_6O_{24}$ pellet was successfully used for fabrication of a solid-state Mg-sensor for measuring Mg concentration in molten Al at 700±5°C, with biphasic powder mixture of $MgCr_2O_4$+Cr_2O_3 as ceramic reference electrode in air. A linear dependence of emf on logarithm of Mg concentration was obtained. The results indicate that the transport number of Mg^{2+}-cation in $MgZr_4P_6O_{24}$ is 0.85±0.03 at 700°C. The solid electrolyte has likely applications in high-temperature electrochemical sensors.

The plethora of research interest in functional materials and characterisation is geared towards understanding the behaviour of engineering materials in operation. Today, materials function optimally in ambient and high-temperature environment, as a result, appropriate materials are selected for certain applications. Selecting materials for high-temperature application invariably requires stability of the materials as well as environmental suitability compared to applications at ambient temperatures. Selection of functional materials for high-temperature application in aggressive environment is extremely challenging.

Aluminium (Al) and magnesium (Mg) are two important light weight structural metals that offer tremendous weight saving potential in automobiles, aerospace and defence application; they both possess the lightest density of common structural materials (ρ_{Al} = 2.77 gcm^{-3}, ρ_{Mg} = 1.74 gcm^{-3}).[1-3] The non-heat-treatable Al-Mg alloys have wide ranging application in the aerospace sector whereas, the age-hardened Al-Mg-Si alloys have shown tremendous combination of strength and formability needed in automobiles.[2]

Production of Al and Mg from raw materials is extremely energy intensive process. Recycling and recovery of Al and Mg from their alloy scrap require only a fraction of that energy. Since the Al-alloy scrap generally contains excess Mg which is demagged during recycling[4], an in-line solid-state Mg-sensor could substantially improve efficiency. Continuous monitoring the composition of the Mg in Al-Mg, Al-Mg-Si and other non-ferrous alloys during recycling and alloying operation, allows in-process adjustments to the alloy composition.[5]

Magnesium ion conducting $MgZr_4P_6O_{24}$ ceramic has attracted attention as a solid electrolyte with potential applications in high-temperature electrochemical sensor for liquid metals and alloys, and other electrochemical devices. $MgZr_4P_6O_{24}$ and other divalent Mg^{2+}-conducting solid electrolytes have been studied.[6-10] In a similar study[11,12], it was reported that the $MgZr_4P_6O_{24}$ divalent cationic conductor belong to β-$Fe_2(SO_4)_3$-type structure possessing three-dimensional skeletal structure comprising PO_4 tetrahedra sharing corners with ZrO_6 octahedra.[10] Recently, the Mg^{2+}-conducting behaviour of $MgZr_4P_6O_{24}$ electrolyte was prepared by a modified sol-gel chemical method and the electrical properties characterised using impedance spectroscopy.[13] The ionic conductivity of $MgZr_4P_6O_{24}$ solid electrolyte, like the Li-ion conductivity which plays a pivotal role in determining the performance of Li-S batteries, and the effect of temperature on ionic conductivity has been proved to be significant for ceramic electrolytes.[14] For example, at 725°C, the ionic conductivity of $MgZr_4P_6O_{24}$ solid electrolyte[13] is of the order of 10^{-3} Scm^{-1}, which shows that the dependence of conductivity on temperature for ceramic electrolytes generally follows a continuous Arrhenius trend.[14] In this study, however, sol-gel method was followed since it is believed to be an excellent method for synthesising precursor oxides of high purity and uniform composition. Adamu and Kale[13] in a recent study identified the potential advantages of sol-gel chemical method over conventional solid-state reaction such as greater homogeneity, compositional control flexibility and lower processing temperature. Among solid electrolytes, it has been discovered that ceramic electrolytes form significant class of materials, as they display a wide range of electrochemical stability window, absence of leakage when compared to liquid electrolytes and they can be fabricated into a variety of sizes and shapes[15,16] having an ordered structure.[17]

Nanoparticles have been used in the synthesis of solid electrolytes for the development of electrochemical sensors owing to their unique physiochemical characteristics[18], although metal nanoparticles like gold and platinum are widely used in specific low temperature sensors, but sensors based on the noble metals are less cost effective for commercial applications at elevated temperatures in aggressive environments.[19] More so, the electrochemical Mg-sensor characterised in this study is aimed at utilising the advantages of electrochemical technologies in the sensing of Mg concentrations in the molten non-ferrous alloys containing Mg.[20]

In fabricating and testing the characterised high-temperature solid-state Mg-sensor, stability of the solid-state Mg-sensor was determined in molten Al and Mg-Al alloys, respectively, at 700±5°C. Sensor sensitivity and its low detection limit, selectivity, and reproducibility of the solid-state Mg-sensor are considered vital to be investigated.[21] Operational stability of the oxide-based electrochemical sensor characterised in this study, like the oxidase-based biosensors, is of particular importance as it significantly improves the sensor performance and applicability in the relevant environment.[22] One requirement for electromotive force (emf) measurements is that both the electrolyte and electrodes are chemically stable in the operating environment.[23] Thus, emf measurements can be conveniently used to measure the more active element in an alloy, as illustrated in this study where the activity of Mg has been measured in molten Al. In general, recent development in sensor technology has evolved as a result of advanced method of synthesising and processing novel functional materials[13,24], exhibiting enhanced electrochemical properties.

Experimental Details

Materials preparation - In preparation of $MgZr_4P_6O_{24}$ solid electrolyte, a simple sol-gel chemical procedure modified by Adamu and Kale[13] was followed. This chemical synthesis route produce very fine and pure nanopowders; achieved through mixing on atomic scale by combining aqueous solutions of soluble salts at a relatively low crystallisation temperature and, it produce compositions not always possible by the solid-state fusion method. The starting reagents in this study were $MgCO_3$ (Sigma-Aldrich, ≥ 40% MgO), Aqueous HNO_3 (Sigma-Aldrich, ACS reagent, 70%), $ZrOCl_2.8H_2O$ (Sigma-Aldrich, 98.5% purity) and $NH_4H_2PO_4$ (Alfa Aesar, 98% purity). All raw materials were weighed in stoichiometric proportions and dissolved in deionised H_2O, better outlined in Figure 1. Aqueous solutions of $Mg(NO_3)_2$ and $NH_4H_2PO_4$ were prepared separately and mixed together while stirring in a beaker to form the homogeneous sol. Further, appropriate amount of aqueous $ZrOCl_2.8H_2O$ solution was prepared and added dropwise to the homogeneous sol using a burette to precipitate acidic whitish gel. To neutralise the mixture, NH_4OH was gradually added dropwise to the homogeneous gel to adjust pH of the gel from 1.2 to a final pH of 10.2. The final solution was stirred for 1h and dried at 100°C for 24h on a hot plate to achieve a dry xerogel. After drying, the dry xerogel powders were mechanically ground with agate mortar and pestle and calcined at 900°C (heating/cooling rate, $\beta = 10^{o}C\ min^{-1}$) to produce single phase polycrystalline whitish $MgZr_4P_6O_{24}$ nanopowders. The calcined nanopowders were mixed with 1 wt.% binder (Ciba Glascol HA4: Ciba speciality Chemicals, Bradford, UK) and then pressed into pellets of 13mm diameter and 3.8mm thickness with a uniaxial steel die at 5kN compressive pressure. The resultant pellet was sintered for 24h at 1300°C (heating/cooling rate, $\beta = 10^{o}C\ min^{-1}$) in a closed alumina crucible immersed in powder of the same composition. Prior to reaching the sintering temperature of the samples, the binder is burnt out between 400 and 450°C.

Materials characterisation - To determine an optimum calcination temperature for $MgZr_4P_6O_{24}$ dry gel powders, simultaneous DSC-TGA was performed on $MgZr_4P_6O_{24}$ dry xerogel powders. The thermal oxidation behaviour and weight loss of the dried gel powders were determined by STA 8000 (PerkinElmer, Seer Green, UK) in order to ensure effective optimisation of calcination conditions of the dried gel powders in a controlled atmosphere at a flow rate of $50mL\ min^{-1}$ using a constant heating/cooling rate, $\beta = 10^{o}C\ min^{-1}$ between 30 and 1000°C. For phase analysis, calcined powders and sintered pellets of $MgZr_4P_6O_{24}$ were examined using powder X-ray diffractometer (Bruker D8 advance, Karlsruhe, GmbH) equipped with Cu K_{α} (with $\lambda = 1.5406Å$) radiation source operating at 30kV and 45mA and calibrated against Si standard. XRD data was collected over $10^{o} \leq 2\theta \leq 80^{o}$ scan range. The unit-cell lattice parameters of the calcined powder and their Rietveld fits were determined using program GSAS[25] with EXPGUI interface.[26] For measurement of electrical properties, sintered $MgZr_4P_6O_{24}$ solid electrolyte pellets were mildly ground to achieve a flat surface without significantly altering the pellet thickness. Platinum paste (Sigma-Aldrich, UK) was lightly applied to the opposite parallel faces of the sintered pellet and allowed to dry before firing in a tube furnace at 800°C for 0.5h to form contact electrodes. The electrical conductivity was recorded as a function of temperature and frequency using impedance analyser, Solartron SI1260 FRA (Hampshire, UK) in the temperature range from 197 to 764°C and frequency range from 100mHZ to 32MHz. Microstructural examinations were performed on carbon-coated fractured pellet using scanning electron microscopy, SEM (Carl Zeiss EVO MA15, Jena, GmbH) equipped with energy-dispersive X-ray spectroscopy and Oxford Aztec X-Act EDS spectrometer. After following standard procedure of sample preparation, TEM (FEI Titan^3 Themis 300, Cambridge, UK) was used to determine surface morphology, crystalline phase, lattice fringes and elemental composition of $MgZr_4P_6O_{24}$ sample. Precision location of component elements in $MgZr_4P_6O_{24}$ were also identified using the TEM fitted with high-angle annular dark field (HAADF) detector operated at an accelerating voltage of 300kV equipped with energy dispersive X-ray spectroscopy (EDS, Oxford INCA 350). The TEM data were analysed using Velox application software.

Sensor fabrication and testing - The general fabrication process of solid-state Mg-sensor is outlined in Figure 2. A simple Mg-probe was firstly produced using a 13mm diameter and 3.8mm thickness sintered composite solid electrolyte pellet attached to an open end of a 50.8mm long alumina tube using pure alumina refractory cement (Parkinson-Spencer Refractories Ltd., Halifax). A 0.25mm thick annealed Fe-Cr alloy wire (Goodfellow, Cambridge) was coiled, inserted and rammed down into bottom of the alumina tube along with a biphasic mixture of $MgCr_2O_4$+Cr_2O_3 which served as the reference electrode. The solid-state Mg-probe was extended by inserting it into a

120mm ceramic tube and holding it firm with an alumina refractory cement to form a bulk solid-state Mg-sensor. Under a purified argon gas environment, the solid-state Mg-sensor was immersed into 560g pure molten Al and eutectic mixture of NaCl and KCl salts at 700±5^{o}C held in a high density alumina crucible. The thin layer of salt-melt protected molten Al from oxidation. A 350mm long and 2mm diameter Mo-rod (Goodfellow, Cambridge) sheathed inside an alumina tube and sealed at both ends, served as an electrical lead to molten Al. The annealed Fe-Cr alloy wire extension from the reference electrode of the Mg-sensor was then connected to the positive terminal of a 10-channel Keithley 6517 A digital electrometer while the Mo-rod was connected to the negative terminal ensuring continuous recording of the cell voltage and temperature of the metal by a computer-controlled multi-channel high-impedance ($\geq 10^{13}\Omega$) electrometer. After long equilibration of the Mg-sensor in pure molten Al to determine the test baseline, change in Mg content in molten Al during the tests was made *in situ* by adding Mg wrapped in Al foil to the pure metal in regulated steps in the range from 0.005 to 1.5wt. % Mg. The temperature was monitored using the K-type thermocouple inserted in the top-loading Lenton LTF 1600 muffle furnace connected through NI USB-TC01 temperature input device (Business Park, Newbury) to LabVIEW interface monitoring real time temperature as shown in Figure 2. When the emf became stable after each Mg addition, suction samples were withdrawn from the melt using a silica tube of 2mm diameter. The Mg concentration of the samples was determined with the Atomic Absorption Spectrometer (AAS), Aanalyst 400 (PerkinElmer, Waltham, USA). The magnesium sensor fabricated in this study is based on the basic principle similar to the potentiometric antimony sensor with the difference that the latter requires an oxide-ion conducting solid electrolyte.[23]

Results and Discussion

Simultaneous DSC - TGA - The thermal behaviour of $MgZr_4P_6O_{24}$ xerogel powders was earlier studied by Adamu and Kale[13], with measurements ranging from 30 to 1000^{o}C, showing a mass loss and thermal decomposition of the dried xerogel powders in flowing air at 50 cc min^{-1} and heating rate of 10^{o}C min^{-1}. It was reported that the TGA curve shows progressive mass loss of the dried xerogel powders in the range from 30 to 500^{o}C and stabilisation between 750 and 870^{o}C. The mass loss from 99.9% to 62.65% and the associated endothermic peaks are attributed to loss of H_2O and decomposition of precursor materials such as $NH_4H_2PO_4$, $Mg(NO_3)_2$, $ZrOCl_2.8H_2O$. $NH_4H_2PO_4$ decomposes to P_2O_5, H_2O, and NH_3 at 190^{o}C, $Mg(NO_3)_2$ to MgO, NO_2, and O_2 at 330^{o}C, and $ZrOCl_2.8H_2O$ to ZrO_2, HCl, and H_2O at 437^{o}C. The exothermic peak between 870 and 900^{o}C signals the formation of $MgZr_4P_6O_{24}$ from reactive oxides MgO, P_2O_5, and ZrO_2 formed *in situ*. The precursor residues, namely NH_4Cl, HCl, HNO_3, and H_2O indicated in Equation (1), vaporise during calcination enabling the formation of pure single phase $MgZr_4P_6O_{24}$.

$$Mg(NO_3)_2\,(aq) + 4ZrOCl_2.8H_2O\,(aq) + 6NH_4H_2PO_4\,(aq)$$
$$= MgZr_4P_6O_{24}\,(s) + 6NH_4Cl\,(aq) + 2HCl\,(aq) + 2HNO_3\,(aq) + 36H_2O\,(l) \quad (1)$$

X-ray diffraction - The formation temperature of the $MgZr_4P_6O_{24}$ indicated by the simultaneous DSC-TGA analysis was confirmed by high-temperature XRD (HT-XRD). XRD patterns of nanopowder calcined at 900°C and pellets sintered at 1300°C have been reported.[13] The pattern of calcined nanopowders agreed well with that of monoclinic $Mg_{0.5}Zr_2(PO_4)_3$ [ICDD-04-016-0487] which shows a single phase. The sintered pellet however shows the presence of minor coexistent second phase, evident for example at 22.54° 2θ. The minor phase is identified as orthorhombic $Zr_2(PO_4)_2O$ [ICDD-04-011-6948]. Hence, the pellet sintered at 1300°C may be considered as a composite solid electrolyte based on $MgZr_4P_6O_{24}$. These findings are consistent with the observations of Pet'kov *et al.*[7] and Kazakos-Kijowski *et al.*[27] When heated in the temperature range $1350 \leq T/^{o}C \leq 1500$, $MgZr_4P_6O_{24}$ is found to decompose to orthorhombic $Zr_2P_2O_9$ and a liquid phase. The composition of the liquid phase changes with sintering temperature and time because of the vaporisation of P_2O_5. As calcination temperature increases from 800 to 900°C, the average crystallite size obtained using Scherrer equation[28-31] also increases from 32±2 nm to 39±2 nm. The pellets sintered at 1300°C shows an optimum density from densification analysis of sintered pellets as a function of temperature.

The XRD pattern at 25°C of the nanopowder calcined at 900°C was refined (Figure 3). The refined parameters and corresponding R-factor are presented in Table 1. Atomic coordinates, site occupancies and displacement parameters are given in Table 2. The crystal structure and lattice cell parameters agree well with those in ICDD-04-016-0487: a(Å) = 12.4218(2), b(Å) = 8.9025(2), c(Å) = 8.8218(2), β(deg) = 90.4660(1), V($Å^3$) = 975.53(2). The differences in unit cell parameters are quite minimal.

HR-TEM of $MgZr_4P_6O_{24}$ nanopowders - The particle morphologies and lattice crystal structures of $MgZr_4P_6O_{24}$ nanoparticles was investigated using high-resolution TEM (HR-TEM) and corresponding SAED. The micrograph in Figure 4 shows two different lattice fringes attributed to [21-2] and [110] interplanar spacing of $MgZr_4P_6O_{24}$ nanoparticles with some amorphous layer surrounding the crystalline particles. The crystal lattice fringes corresponding to 3.9038Å and 5.6820Å atomic spacing, are characteristics of monoclinic $MgZr_4P_6O_{24}$. The d-spacing of the surface grafting nanoparticles in Figure 4(ai) and Figure 4(aii) shows trend of core crystallinity. The SAED pattern in Figure 4(aiii) can be indexed to the (100) zone axes of monoclinic $MgZr_4P_6O_{24}$, testifying to homogeneity and pure single phase of the nanoparticles. The d-spacing values obtained from SAED patterns in Figure 4(aiii) compares well with the XRD data achieved in this study, comparable with an earlier study.[13]

Figure 5 depicts the corresponding elemental map of $MgZr_4P_6O_{24}$ nanopowders. The spectra in the maps show uniform spatial distribution of Mg, Zr, P, and O with the corresponding atomic ratio in $MgZr_4P_6O_{24}$ indicating homogeneous phase as evident in Figure 10 which agrees with XRD patterns in this study as presented in Table 3.

Table 3 shows EDS spectrum of $MgZr_4P_6O_{24}$ nanoparticles with non-stoichiometric concentration. For instance, dividing through by 2.73 shows less concentration of Zr while, P and O are in excess of standard concentration. However, the nanoparticles shows uniformity in terms of spatial distribution of the maps.

Electrical conductivity - Impedance analysis - Fast ionic conductors attract attention as an indispensable material for the development of next generation energy systems, chemical sensors and other electrochemical devices.[32] For the ionic conductivity, a pure single phase electrolyte powder with a high surface area is required.[33] However, to incorporate this material as a solid electrolyte in fabricating electrochemical sensor, highly dense sintered ceramic is needed.[33] The results of impedance analysis of the $MgZr_4P_6O_{24}$ pellet obtained by two-probe method in the temperature range from 197 to 764°C and frequency range from 100mHz to 32MHz are presented in Figure 6 showing electrical properties of the solid electrolyte which qualifies it as Mg^{2+} - cationic conductor. The ac-impedance method allows contribution from the grain interior, grain boundaries, and electrode-electrolyte interface to electrical conductivity of the sample. Figures 6(a) and 6(b) demonstrates impedance measurements at both low and high-temperatures with the electric modulus showing various relaxation points at different temperatures suggesting a conduction mechanism which is a thermally activated type of correlated hopping of Mg^{2+}-cations. The impedance spectra in Figure 6(a) however shows a single slightly depressed semicircle at higher frequency followed by the low-frequency spike inclined at 45°, and the border frequency, f_b separating both the high and low-frequency regions, was observed at frequency region 50.7 kHz and 12.7 kHz, respectively, for low and high-temperature impedance analysis. The inclined spike at low frequencies of $MgZr_4P_6O_{24}$ solid electrolyte shows it as cationic conductor[34,35] and the slightly depressed semicircle attributed to constant phase element (CPE) parameter appears to suggest the non-Debye relaxation type[36], similar to solid electrolytes studied earlier[37] since the centre of the depressed semicircle is located below the real axis. However, the inclined spike in low-frequency region may be attributed to the polarisation effect at the electrode-electrolyte interface.[38] The semicircle in Figures 6(a) and 6(b) can be expressed in terms of an equivalent circuit built from a combination of resistance, R_p and capacitance, C_p with a CPE[39] relation as;

$$Z = \frac{1}{C(j\omega)^n} \tag{2}$$

Using the CPE relation in equation (2), C representing an ideal capacitance iff n =1, j = $(-1)^{1/2}$ and ω is the angular frequency. In real terms, the equivalent circuit consists of a series combination of parallel RC circuit elements and a series resistor, R_s. Grain resistance denotes a lumped resistance, while grain boundary resistance is represented by a resistance attached in parallel to a capacitor.[40]

As impedance analysis temperature increases from 390 to 764°C, the depressed bulk semicircle gradually became smaller relative to the inclined spike. This shows that as bulk resistance, R_b is decreasing, the reversibility of charge migration of the electrode-electrolyte, interface is increasing.[41] The semicircle in Figure 6(b) however, started off the origin indicating there is a finite resistance, R_s representing lumped electrode-electrolyte interfacial resistance in series with a parallel combination of R_b and CPE_b which represents a grain resistance and constant phase element as presented in Figure 6(c);

The capacitance, C of the solid electrolyte was calculated at different temperature as outlined in Figure 6, using frequency, f at the maximum point of the semicircle. In using the relation, $C = (2\pi fR)^{-1}$ where f and R represent the frequency and resistance of electroceramics, the capacitance and related interpretation is outlined in Table 4:

Temperature dependence of ac-conductivity - The linearity plot presented in Figure 7 shows ionic conductivity of $MgZr_4P_6O_{24}$ solid electrolyte at different temperature. The linearity of the plot suggests there is no significant phase changes within 197-764°C temperature range of measurement. This also suggest $MgZr_4P_6O_{24}$ solid electrolyte as a good ionic conducting material. The activation energy, E_a was determined from the gradient of Arrhenius plot by fitting the ac-conductivity data with the Arrhenius equation as presented;

$$\sigma T = A\exp\left(-\frac{E_a}{kT}\right) \tag{3}$$

Where σ is the total conductivity, A is the pre-exponential factor, E_a is the activation energy for conduction, k is the Boltzmann constant and T is temperature (K).

Based on the relation between equation (3) and the data of this study, ionic conduction as a thermally activated transport, shows that conductivity increases exponentially as temperatures increase. In this study therefore, the $MgZr_4P_6O_{24}$ solid electrolyte shows a bulk conductivity of 7.23×10^{-3} Scm^{-1} at 725°C, which is a slight improvement on 6.92×10^{-3} Scm^{-1} at 800°C achieved in an earlier study.[42] The activation energy, E_a of the solid electrolyte, calculated from the slope of $\ln\sigma_{dc}T$ - $1000T^{-1}$ plot in Figure 7 equates to 0.84±0.04eV. It shows $MgZr_4P_6O_{24}$ solid electrolyte with low E_a which of course provides a shorter profile of Mg^{2+}-cationic mobility thereby resulting in an improved conductivity.

Frequency dependence of ac-conductivity – Frequency dependence of the real impedance (ReZ) for $MgZr_4P_6O_{24}$ solid electrolyte at different temperatures is presented in Figure 8. The ac-conductivity dispersion plots of $MgZr_4P_6O_{24}$ solid-state electrolyte shows three regions of interest (i) low-frequency dispersion, (ii) intermediate-frequency plateau, and (iii) extended dispersion at high frequency.[43-46]

The low-frequency dispersions in ac-conductivity correspond to electrode polarisation at the electrode-electrolyte interface.[38] At this frequency, the ionic conductivity of $MgZr_4P_6O_{24}$ is high enough to accumulate a significant amount of charge at the electrode-electrolyte interface, which reduces the effective applied field across the measured sample resulting in possible conductivity.[47-49]

Intermediate-frequency plateau represents the dc-conductivity and does not depend on frequency, but on temperature, which agrees excellently with conductivity relationship in Figure 8. The switch over from the intermediate-frequency region to the extended dispersion region at high frequency signals the onset of conductivity relaxation, which shifts toward higher frequencies as the temperature increases, representing ac-ion conductivity. The observed dispersion of this conductivity with frequency agrees with the prediction of the jump relaxation model in solid electrolytes.[50] According to this model, as frequencies tend to zero ($f \rightarrow 0$), ion can jump from one site to another neighbouring vacant site which contributes to ac-conductivity.[50] However, at high frequencies, the probability of the ion to jump back to its initial site increases due to available short time frame. The high probability for the correlated forward-backward hopping at high frequencies together with the relaxation of the dynamic cage potential is responsible for the high frequency dispersion.[51] In any case, since the crossover frequency is temperature dependent, it can be observed in Figure 6 that the crossover frequencies, ω_p, shift towards high-frequency as temperature increases. Meanwhile, the logarithmic plot between dc-conductivity and crossover frequency, ω_p, in Figure 8 insert gives a slope of 1 which agrees with conductivity formalism[50], which implies that both dc- and ac-conductions are closely correlated and that they are of same mechanism[52], alternatively, the characteristic angular frequency, ω_p, is activated with the same thermal activation energy as dc-conductivity.[49,50,52,53]

At high-frequency dispersion, angular frequency-dependent ac-conductivity, $\sigma_{ac}(\omega)$ increases and is well described by the Jonscher universal power law formulated as[45,54]

$$\sigma_{ac}(\omega) = \sigma_{dc} + A\omega^n \qquad (4)$$

where $\sigma_{ac}(\omega)$ is the ac-conductivity, σ_0 is the limiting zero frequency conductivity (σ_{dc}) of the electrolyte, A is the pre-exponential constant, $\omega = 2\pi f$ is the angular frequency and n is the power law exponent which represents the degree of interaction between the mobile ion and is less than 1 ($0 < n < 1$).[46] The value of n is extracted from the slope of $\log\sigma_{ac}(\omega)$ versus $\log\omega$ when $\sigma_0 \rightarrow$ zero. Furthermore, the conductance spectra in Figure 8 shows that when measurement temperature increases, the transition from the dc-conductivity plateau to ac-conductivity dispersion region shifts towards higher frequency range (10^3–10^7 rad/s). At high frequencies, the conductance spectra at different temperatures converge thus indicating that ac-conductivity is independent of temperature at high frequencies.[55-58]

A comparison of dc-conductivity from the intermediate-frequency plateau with ac-conductivity using Arrhenius relation is presented in Figure 9. The close correlation in the total conductivity depicts that the conduction is from the same majority charge carrier, Mg^{2+}-cation, and that the composite solid electrolyte is purely ionic. This equally suggest a reasonably high transference number for Mg^{2+}-cation in $MgZr_4P_6O_{24}$ solid electrolyte as well as their comparable activation energy, $E_a(ac) = 0.84\pm0.004eV$ and $E_a(dc) = 0.87\pm0.004eV$.

SEM of fracture surface $MgZr_4P_6O_{24}$ - Figure 10 shows the micrograph of $MgZr_4P_6O_{24}$ fracture surface ceramic pellet sintered at 1300°C. It is clear that the pellet analysed in this study shows a dense structure with little porosity which is in perfect agreement with an optimum relative density of ~ 99% achieved at 1300°C for the solid electrolyte. The relative density is determined from the physical dimensions and theoretical density calculated from crystal structure of the electrolyte. The EDS spectrum (i) as presented in Table 5 indicates the ceramic pellet homogeneity, and the elemental composition is of stoichiometric concentration. The elemental ratio Mg, Zr, P, O in the selected region agrees with the anticipated stoichiometric composition of $MgZr_4P_6O_{24}$.

Sensor for Mg in liquid Al - Sensor testing - The solid-state Mg-sensor designed in this study can be schematically represented as:

$$(+)\ \text{air, Fe-Cr, } MgCr_2O_4+Cr_2O_3(s)/MgZr_4P_6O_{24}(s)/Al\text{-}Mg(l),\ Mo\ (-) \qquad (5)$$

The measured open circuit voltage of the sensor at different Mg concentrations is given in Table 6 and can be represented by equation (6):

$$E/V\ (\pm0.009) = 2.446 + 0.1265\ \log X_{Mg} \qquad (6)$$

The voltage generated between the dissimilar metal leads from the two electrodes (Mo(+) – Fe-Cr(-)) at 700±5°C measured independently is -0.0093V. The emf of the cell corrected for thermo-emf is given by:

$$E/V\ (\pm0.009) = 2.437 + 0.1265\ \log X_{Mg} \qquad (7)$$

Figure 11(a) shows the response of Mg-sensor to changes in the concentration of Mg in molten Al using $MgCr_2O_4+Cr_2O_3$ biphasic powder mixture as the reference electrode. Each step in Figure 11(a) correspond to the addition of Mg in molten Al at 700±5°C. It shows that the sensor emf increases with the concentration of Mg in molten Al. The sensor response was rapid. The emf response as a function of time in Figure 11(a) suggests that the solid electrolyte is chemically stable in molten Al at 700±5°C. Meanwhile, instability in the sensor signal at 0.005 wt.% Mg in molten Al could in part be due to the possibility of reaching a limiting value for the measurement of Mg in molten Al using $MgZr_4P_6O_{24}$ as solid electrolyte.[59,60] Figure 11(b) shows sensor voltage variation of the solid-state Mg-sensor in molten Al at 700±5°C. The measured voltage variation of this solid-state Mg-sensor as a function of concentration of Mg in molten Al at 700±5°C is in general agreement with the earlier findings.[59,60]

The activity of Mg is relatively high at the alloy electrode and very low at the ceramic electrode exposed to air. The electrochemical reaction at the alloy electrode on the right-hand side of the cell is:

$$\{Mg\}_{Al(l)} \rightarrow Mg^{2+} + 2e^- \quad (8)$$

At the reference electrode on the left-hand side, the electrochemical reaction is:

$$Mg^{2+} + 0.5O_2(g) + Cr_2O_3(cor) + 2e^- \rightarrow MgCr_2O_4(sp) \quad (9)$$

The emf (E/V) of the sensor is given by the expression

$$E = -\frac{1}{nF}\int_{\mu_{Mg}^{ii}}^{\mu_{Mg}^{i}} t_{ion} d\mu_{Mg} \quad (10)$$

Where F is the Faraday constant in Coulombs mol^{-1}, n = 2 is the number of electrons participating in the electrode reactions, t_{ion} is the transport number of the conducting species (Mg^{2+}), and μ_{Mg} is the chemical potential of Mg defined as $RT\ln a_{Mg}$ where a_{Mg} is the thermodynamic activity of Mg, the neutral form of the conducting species in the electrolyte. It is apparent from the polarity of the cell and emf response of the sensor that, the chemical potential of Mg at the reference electrode (μ^{ii}_{Mg}) is lower than that at the molten alloy sensing electrode (μ^{i}_{Mg}).

If it is assumed that the transport number of Mg^{2+}-cation in $MgZr_4P_6O_{24}$ is unity, emf of Mg-sensor can be calculated from the thermodynamic activity of Mg in molten Al. The Gibbs energy of formation of $MgCr_2O_4$(sp) from its component binary oxides according to Jacob[61] is given by

$$MgO(rs) + Cr_2O_3(cor) = MgCr_2O_4(sp) \quad (11)$$

$$\Delta G^o_{f(ox)} (\pm 400)/Jmol^{-1} = -45{,}200 + 5.36(T/K) \quad (12)$$

At 700°C (973K);

$\Delta G^o = -39985 Jmol^{-1}$. Combining this with the Gibbs energy of formation of MgO at the same temperature

$$Mg(l) + 0.5O_2(g) = MgO(s),\ \Delta G^o_f = -501401 Jmol^{-1} \qquad (13)$$

The Gibbs energy change associated with the virtual cell reaction at 700°C is given by;

$$Mg(l) + Cr_2O_3(cor) + 0.5O_2(g) = MgCr_2O_4(sp),\ \Delta G^o = -541386 Jmol^{-1} \qquad (14)$$

The estimated uncertainty in the value of Gibbs energy change for reaction (14) is 5 $Jmol^{-1}$. EMF of the sensor is related to the activity of Mg in molten Al by the relation;

$$-2FE = \Delta G = \Delta G^o + RT\ln a_{Mg} + 0.5RT\ln p_{O2} \qquad (15)$$

Thus, the theoretical emf of the sensor at 700°C can be calculated as;

$$E_{th}(\pm 0.026)/V = 2.7728 + 0.09653\log a_{Mg} \qquad (16)$$

Aghdam and Soltanieh[62] measures activity of Mg in liquid Al using an electrochemical cell with the eutectic mixture of $MgCl_2$-$CaCl_2$ as an electrolyte in a temperature range from 700 to 800°C and Mg composition from 0.07 to 12.1. The activity coefficient of Mg at 700°C for dilute alloys up to 1.4 atom % Mg can be expressed by the relation,

$$\log\gamma_{Mg} = -0.7624 + 23.183X_{Mg} \qquad (17)$$

Expressing activity of Mg in Equation (16) as a product of mole fraction and activity coefficient, one obtains;

$$E_{th}(\pm 0.03)/V = 2.6992 + 2.2379X_{Mg} + 0.09653\log X_{Mg} \qquad (18)$$

The theoretical emf is compared with the measured values in Figure (12). On the average, the measured values are lower by ~0.359±0.022V. The average transport number at 700°C for Mg^{2+}-cations over the range of chemical potential at the two electrodes can be computed from the difference between experimental and theoretical emfs assuming that the electrodes are not polarised.

$$t_{ion} = \frac{E_{exp}}{E_{th}} \tag{19}$$

The average transport number for Mg^{2+}-cations in the $MgZr_4P_6O_{24}$ solid electrolyte obtained thus is shown in Figure 13 as a function of Mg concentration. The average value is 0.85±0.03.

The results in this study however compares favourably with the activity of Mg in liquid Al reported by Aghdam and Soltanieh.[62] However, it is quite likely that the measured emf is affected by the relatively large electron-hole transport in the electrolyte and the large difference in chemical potential of Mg at the two electrodes leading to polarisation of the solid reference electrodes. Hence, the testing of $MgZr_4P_6O_{24}$ solid electrolyte with other reference electrodes with higher Mg chemical potential is recommended.

Conclusions

According to TGA - DSC analysis and XRD data, the xerogel powder formed during sol-gel synthesis transformed to pure single-phase monoclinic $MgZr_4P_6O_{24}$ after calcination at 900°C. HR-TEM measurements also confirmed the formation of $MgZr_4P_6O_{24}$ in the range $900 \leq T/°C \leq 1300$. Rietveld refinement was used to access the crystal structure parameters of $MgZr_4P_6O_{24}$. EDS spectra confirmed that the spatial distribution of the constituent elements agree with the corresponding atomic ratio of the complex phosphate.

Dense and stable sample pellets for impedance analysis were prepared by room temperature compressive pressure consolidation and sintering of the nano size powder at 1300°C. The electrical properties of $MgZr_4P_6O_{24}$ were determined as a function of temperature using impedance spectroscopy. The compound appears to be Mg^{2+}-cation conductor at high temperatures for electrochemical devices and thermodynamic measurements. Sintered $MgZr_4P_6O_{24}$ was stable at 700±5°C in molten Al and Al-Mg alloys in the range from 0.005 to 1.5wt. % Mg. The $MgZr_4P_6O_{24}$ pellets were used to fabricate a solid-state sensor for measuring Mg concentration in molten Al. A biphasic powder mixture of $MgCr_2O_4$+Cr_2O_3 in air was used as reference electrode. The sensor voltage was a linear function of logarithm of the Mg concentration. Hence a practical sensor can be developed for remelting and casting applications. However, the sensor emf was consistently below the theoretical value suggesting an average ionic transport number of 0.85±0.03 for $MgZr_4P_6O_{24}$ in the temperature and Mg chemical potential range covered in this study.

Acknowledgements

The authors appreciate TETFund for the PhD fund and Dr Jennifer Forrester, Dr Faye Esat, Dr Zabeada Aslam, Mr Stuart Micklethwaite, Mr Mohammed Javed, and Mr Simon Lloyd for technical assistance.

The authors declare no competing financial interest.

ORCID: https://orcid.org/0000-0002-3021-5905

Girish M. Kale
*Email: g.m.kale@leeds.ac.uk

Mohammed Adamu
pmmaa@leeds.ac.uk
ORCID: https://orcid.org/0000-0002-5028-9370

K. T. Jacob
katob@iisc.ac.in
ORCID: https://orcid.org/0000-0002-4498-2742

References

1. W.J. Joost, and P.E. Krajewski, *Scripta Materialia,* **128,** 107-112 (2017).
2. J. Hirsch, and T. Al-Samman, *Acta Materialia,* **61,** 818-843 (2013).
3. H. Friedrich, and S. Schumann, *Journal of Materials Processing Technology,* **117,** 276-281 (2001).
4. B.L. Tiwari, *Journal of the Minerals, Metals, and Materials Society,* **34,** 54-58 (1982).
5. J.W. Fergus, and S. Hui, *Metallurgical and Materials Transactions B,* **26,** 1289-1291 (1995).
6. S. Barth, S. Olazcuaga, and P. Gravereau, *Materials Letters,* **16(2-3),** 96-101(1993).
7. V.I. Pet'kov, V.S. Kurazhkovskaya, A.I. Orlova, and M.L. Spiridonova, *Crystallography Reports,* **47(5),** 736-743 (2002).
8. A. Orlova, G.Y. Artem'eva, and I. Korshunov, *Zhurnal Neorganicheskoi Khimii,* **35(5),** 1091-1094 (1990).
9. S. Ikeda, M. Takahashi, J. Ishikawa, and K. Ito, *Solid State Ionics,* **23(1-2),** 125-129 (1987).
10. K. Nomura, S. Ikeda, K. Ito, and H. Einaga, *Bulletin of the Chemical Society of Japan,* **65(12),** 3221-3227 (1992).
11. K. Nomura, S. Ikeda, K. Ito, and H. Einaga, *Journal of Electroanalytical Chemistry,* **326(1-2),** 351-356 (1992).
12. P.C. Christidis, and P.J. Rentzeperis, *Zeitschrift Fur Kristallographie - Crystalline Materials,* **141,** 233-245 (1975).
13. M. Adamu, and G.M. Kale, The *Journal of Physical Chemistry C,* **120,** 17909-17915 (2016).
14. X. Judez, H. Zhang, C. Li, G.G. Eshetu, J.A. Gonzalez-Marcos, M. Armand, and L. M. Rodriguez-Martinez, *Journal of the Electrochemical Society,* **165(1),** A6008-A6016 (2018).
15. P. Knauth, *Solid State Ionics,* **180,** 911-916 (2009).
16. J.W. Fergus, *Solid State Ionics,* **227,** 102-112 (2012).
17. S. Tamura, A. Mori, and N. Imanaka, *Solid State Ionics,* **175,** 467-470 (2004).
18. Y. Hu, Y. Song, Y. Wang, and J. Di, *Thin Solid Films,* **519,** 6605 (2011).
19. U. Sivasankaran, and K.G. Kumar, *Journal of the Electrochemical Society,* **166(2),** B92-B94 (2019).
20. Y. Liu, H. Li, L. Lu, B. Sun, L. Huang, H. Chen, W. Qiu, J. Tao, and P. Zhao, *Journal of the Electrochemical Society,* **166(2),** B133-B140 (2019).

21. S.M. Ali, and H.A. Al lehaibi, *Journal of the Electrochemical Society,* **165(9),** B345-B350 (2018).
22. E.V. Karpova, E.E. Karyakina, and A.A. Karyakin, *Journal of the Electrochemical Society,* **164(5),** B3056-B3058 (2017).
23. J.W. Fergus, and S. Hui, *Journal of the Electrochemical Society,* **143(8),** 2498 2502 (1996).
24. N.P. Shetti, D.S. Nayak, S.J. Malode, and R.M. Kulkarni, *Journal of the Electrochemical Society,* **164(5),** B3036-B3042 (2017).
25. A.C. Larson, and R.B. Von-Dreele, *Los Alamos National Laboratory Report,* 86-748 (2004).
26. B.H. Toby, *Journal of Applied Crystallography,* **34,** 210-213 (2001).
27. A. Kazakos-Kijowski, S. Komarneni, D. Agrawal, and R. Roy, *Materials Research Bullutin,* **23(8),** 1177-1184 (1988).
28. A.R. Stokes, and A.J.C. Wilson, *Proceedings of the Physical Society,* **56,** 174 (1944).
29. A.R. Bushroa, R.G. Rahbari, H.H. Masjuki, and M.R. Muhamad, *Vacuum,* **86(8),** 1107-1112 (2012).
30. U. Holzwarth, and N. Gibson, *Nature Nanotechnology,* **6,** 534-534 (2011).
31. L. Singh, U.S. Rai, and K.D. Mandal, *Journal of Alloys and Compounds,* **555,** 176-183 (2013).
32. D. Mori, K. Sugimoto, Y. Mastuda, K. Ohmori, T. Katsumata, S. Taminato, Y. Takeda, O. Yamamoto, and N. Imanishi, *Journal of the Electrochemical Society,* **166(3),** A5168-A5173 (2019).
33. A. Paulus, S. Kammler, S. Heuer, M.C. Paulus, P. Jakes, J. Granwehr, and R.A. Eichel, *Journal of the Electrochemical Society,* **166(3),** A5403-A5409 (2019).
34. R.A. Huggins, *Ionics,* **8,** 300-313 (2002).
35. J.T. Irvine, D.C. Sinclair, and A.R. West, *Advanced Materials,* **2,** 132-138 (1990).
36. J.R. MacDonald, Wiley-Interscience, John Wiley and Sons, New York, 1-346 (1987).
37. B.V.R. Chowdari, and R. Gopalakrishnan, *Solid State Ionics,* **18,** 483-487 (1986).
38. P. Ferloni, and A. Magistris, *Journal de Physique IV,* **4,** C1-3-C1-15 (1994).
39. D.F. Zhou, Y.J. Xia, J.X. Zhu JX, and J. Meng, *Solid State Sciences,* **11(9),** 1587-1591 (2009).
40. P. Yadav, and M.C. Bhatnagar, *Ceramics International,* **38,** 1731-1735 (2012).
41. Q.B. Bo, G.X. Sun, and J. Meng, *Journal of Physics and Chemistry of Solids,* **67,** 732-737 (2006).
42. N. Imanaka, Y. Okazaki, and G. Adachi, *Journal of Materials Chemistry,* **10,** 1431-1435 (2000).
43. A.K. Jonscher, *Colloid and Polymer Science,* **253(3),** 231-250 (1975).

44. A.K. Ivanov-Schitz, and A.B. Bykov, *Solid State Ionics,* **100,** 153-155 (1997).

45. A.K. Jonscher, *Journal of Materials Science,* **16,** 2037-2060 (1981).

46. M.D. Ingram, *Physics and Chemistry of Glasses,* **28,** 215-234 (1987).

47. M. Sugantha, and M. Varadaraju, *Solid State Ionics,* **95,** 201-205 (1997).

48. C. Mariappan, G. Govindaraj, and B. Roling, *Solid State Ionics,* **176,** 723-729 (2005).

49. G. Govindaraj, and C. Mariappan, *Solid State Ionics,* **147,** 49-59 (2002).

50. K. Funke, *Progress in Solid State Chemistry,* **22,** 111-195 (1993).

51. M. A. Afifi, M. M. El-Nahass, A.E. Bekheet, and I.T Zedan, *Physica B: Condensed Matter,* **400(1-2),** 248-251 (2007).

52. T. Prakash, *International Nano Letters,* **2,** 1-3 (2012).

53. C. R. Mariappan, G. Govindaraj, S. V. Rathan, and G. V. Prakash, *Materials Science and Engineering: B,* **121(1-2),** 2-8 (2005).

54. A.K. Jonscher, *Nature,* **267,** 673-679 (1977).

55. L.P. Teo, M.H. Buraidah, A.F.M. Nor, and S.R. Majid, *Ionics,* **18(7),** 655-665 (2012).

56. M. Vijayakumar, G. Hirankumar, B. Sirakumar, and S. Subramanian, *Journal of Power Sources,* **117(1),** 143-147 (2003).

57. T. Savitha, S. Selvasekarapandian, C.S. Ramya, M.S. Bhuvaneswari, G. Hirankumar, R. Baskaran, and P.C. Angelo, *Journal of Power Sources,* **157(1),** 533-536 (2006).

58. A.M. Abo El Ata, S.M. Attia, and T.M. Meaz, *Solid State Sciences,* **6,** 61-69 (2004).

59. G.M. Kale, L. Wang, and Y. Hong, *International Journal of Applied Ceramic Technology,* **1(2),** 180-187 (2004).

60. G.M. Kale, K.T. Jacob, L. Wang, and Y. Hong, *Transactions of the Electrochemical Society,* **1(13),** 1-11 (2006).

61. K.T. Jacob, *Journal of the Electrochemical Society,* **124,** 1827-1831 (1977).

62. G.R.K. Aghdam, and M. Soltanieh, *Canadian Metallurgical Quarterly,* **49,** 39-45 (2010).

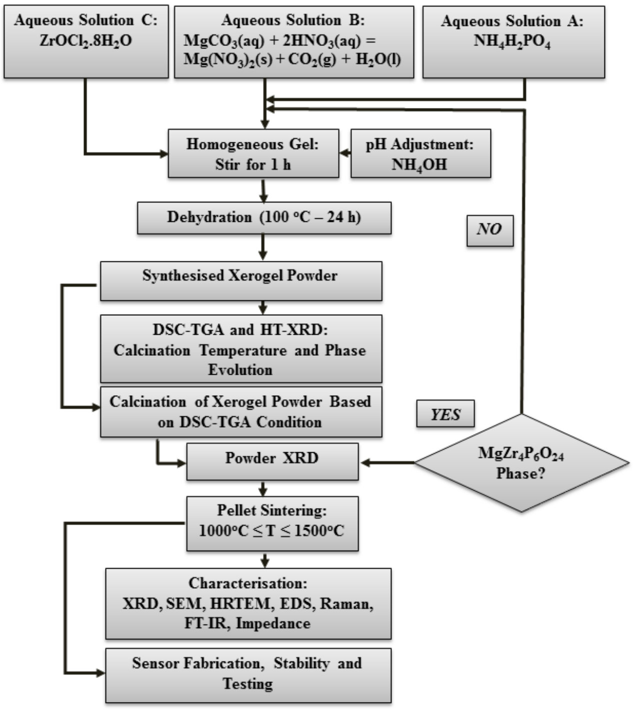

Figure 1. Flowchart showing the sol-gel chemical synthesis procedures

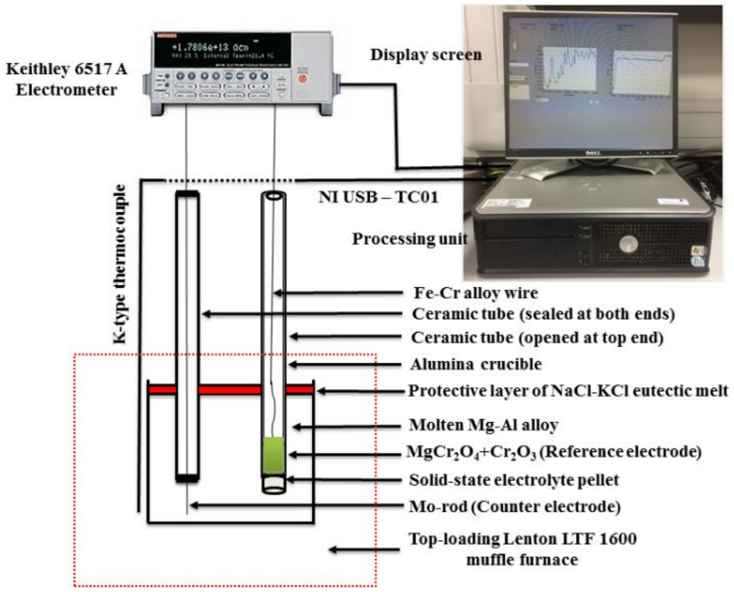

Figure 2. A schematic of the solid-state Mg-sensor test rig.

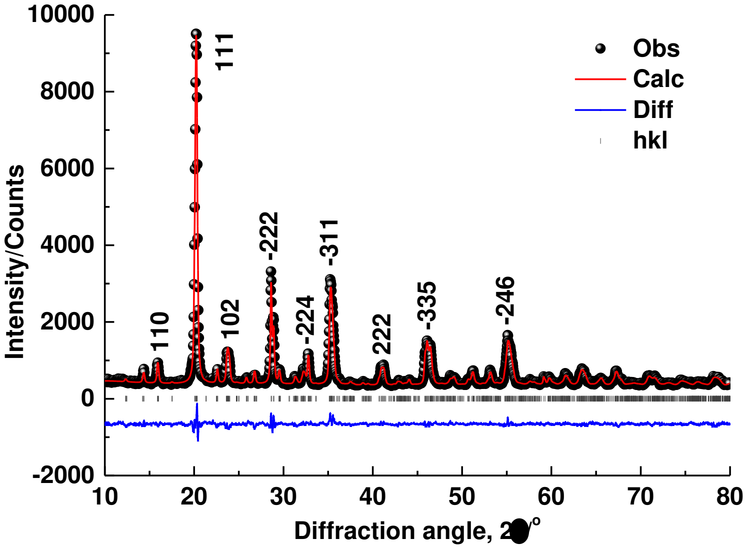

Figure 3. Experimental (black sphere) and calculated (red line) XRD peak profile of $MgZr_4P_6O_{24}$ and the difference between the experimental and calculated spectra (blue bottom line). Dark grey vertical bars indicate allowed Bragg reflection positions of the calculated XRD peaks profile.

Table 1. The unit cell characteristics and results of the Rietveld refinement for the crystal structure of $MgZr_4P_6O_{24}$ sample at 25°C (The standard deviation in units of the last decimal is presented in brackets).

Space group, Z	$P2_{1/n}$, 4
Radiation	CuKα X-ray
Wavelength, Å	1.54056
2θ scan range, deg	10 - 80
Unit cell parameters:	
a, Å	12.3850(8)
b, Å	8.8775(6)
c, Å	8.8001(7)
β, deg	90.529(5)
V, Å^3	967.52(12)
Number of reflections	198
Refinement parameters	18
Residual values, %:	
R_{wp}	5.43
R_p	4.25
χ2	1.680

Table 2. Atomic coordinates, site occupancies q, and displacement parameters of U_{iso}/U_e*100 in $MgZr_4P_6O_{24}$ structures.

Atom	x	y	z	U_{iso}/U_e*100	q
11	0.1616	0.2183	0.7182	12.21	0.6902
Zr(1)	0.1153	0.0293	0.2530	2.52	1.0000
Zr(2)	0.3882	0.0290	0.7466	1.50	1.0000
P(1)	0.4864	0.2846	0.4500	4.92	0.6292
P(2)	0.1481	0.3731	0.3848	5.96	0.7925
P(3)	0.3537	0.3838	0.8720	9.89	0.7905
O(1)	0.5570	0.2953	0.5872	14.61	1.0000
O(2)	0.5768	0.1783	0.3516	4.13	1.0000
O(3)	0.3875	0.3820	0.2995	6.65	1.0000
O(4)	0.4796	0.1333	0.5788	12.41	1.0000
O(5)	0.1918	0.2035	0.3488	7.25	1.0000
O(6)	0.0395	0.4268	0.3542	11.86	1.0000
O(7)	0.1379	0.4241	0.5780	13.63	1.0000
O(8)	0.2024	0.4983	0.2618	9.43	1.0000
O(9)	0.3311	0.2305	0.8198	12.85	1.0000
O(10)	0.3746	0.3586	0.0556	5.56	1.0000
O(11)	0.4529	0.4608	0.8191	2.71	1.0000
O(12)	0.2526	0.5475	0.8331	9.05	1.0000

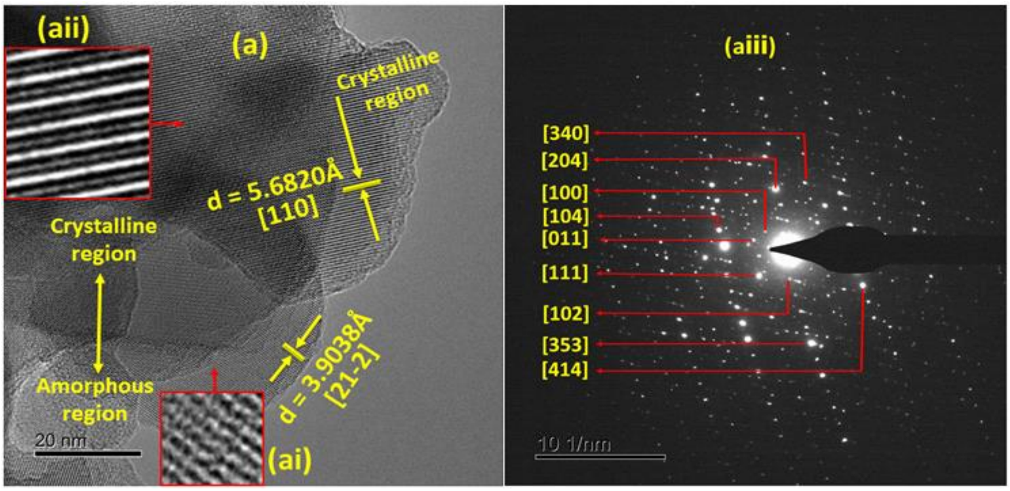

Figure 4. HR-TEM micrograph image and corresponding SAED patterns for (a-aiii) $MgZr_4P_6O_{24}$ nanoparticles prepared by calcining the precursor xerogel at 800°C for 0.5h showing details of d-spacing from lattice fringes of HR-TEM and SAED patterns.

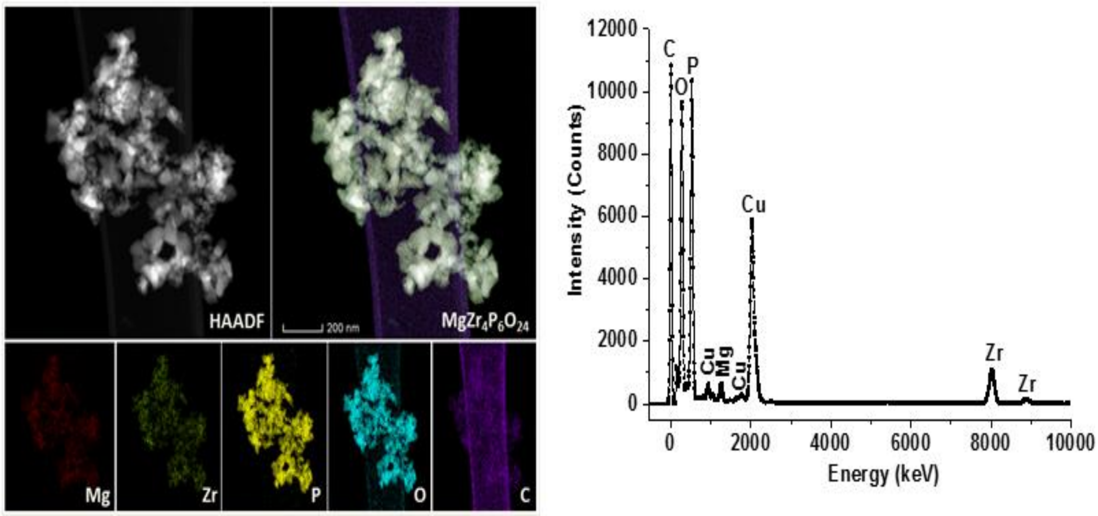

Figure 5. HAADF and EDS elemental maps of $MgZr_4P_6O_{24}$ nanopowders calcined at 800^{o}C for 0.5h.

Table 3. Average elemental composition spectra of $MgZr_4P_6O_{24}$ nanoparticles.

Element	Atomic Fraction (%)	Atomic Ratio
Mg	2.73	1.00
Zr	9.34	3.42
P	17.94	6.57
O	69.99	25.64
Total	100.00	

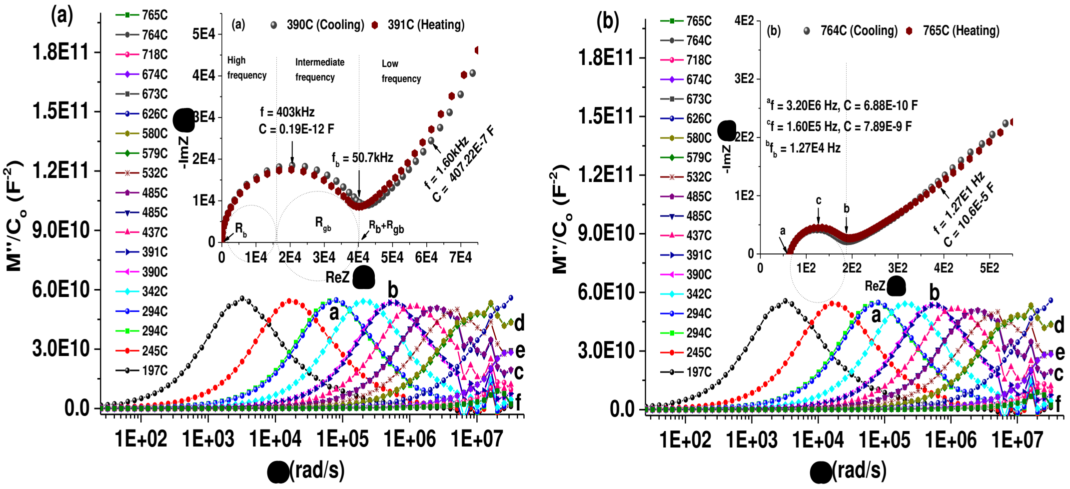

Figure 6. Electric modulus and Nyquist plots of MgZr$_4$P$_6$O$_{24}$ solid electrolyte at (a) 390 and 391°C and (b) 764 and 765°C in 100mHz-32MHz frequency range. *f$_b$ is border frequency of the Nyquist plots. *inscription a-f showing reproducibility behaviour of the solid electrolyte.

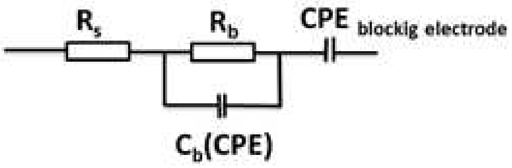

Figure 6(c). The equivalent circuit of MgZr$_4$P$_6$O$_{24}$ sample measured at 390-391°C, and 764-765°C.

Table 4. Capacitance values and their possible interpretation

Solid Electrolyte	Frequency (Hz)	Resistance (Ω)	Capacitance (F)	Phenomenon Responsible [35]
$MgZr_4P_6O_{24}$ (390-391°C)	4.03×10^5	2.08×10^6	0.19×10^{-12}	bulk
45° electrode spike	1.60×10^3	2.44×10^1	407.22×10^{-7}	sample-electrode interface
$MgZr_4P_6O_{24}$ (764-765°C)	3.20×10^6	7.23×10^1	688.0×10^{-12}	bulk
	1.60×10^5	1.26×10^2	7.89×10^{-9}	grain boundary
45° electrode spike	1.27×10^1	11.82×10^1	10.6×10^{-5}	sample-electrode interface

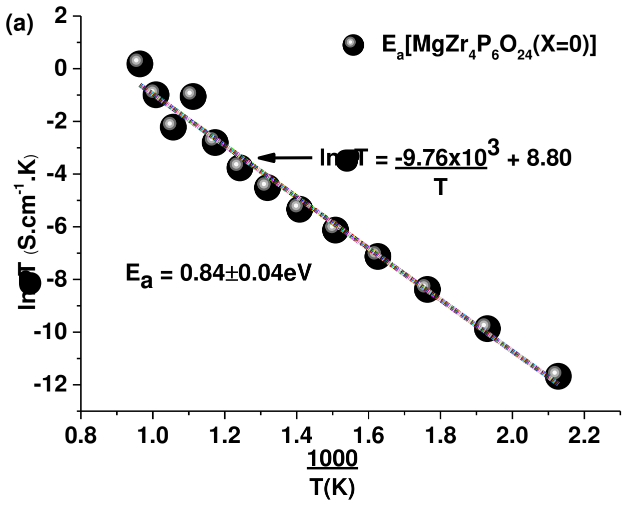

Figure 7. Bulk ionic conductivity of $MgZr_4P_6O_{24}$ solid-state electrolyte as a function of temperature.

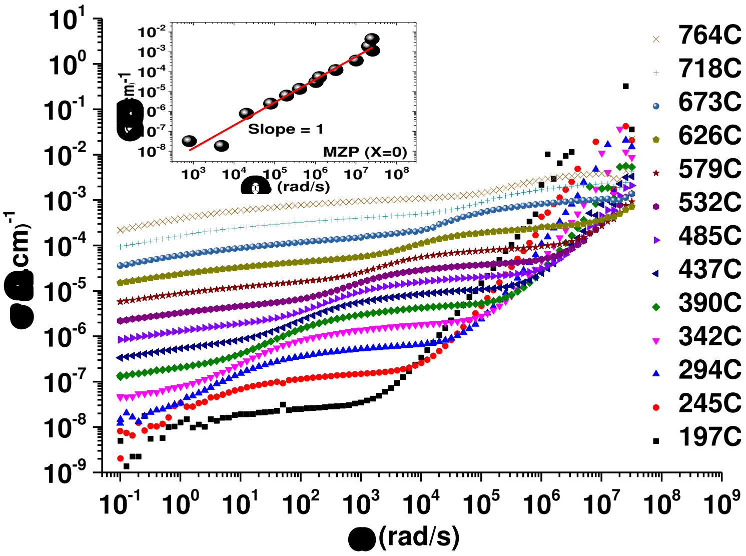

Figure 8. The ac-conductivity dispersion plots of $MgZr_4P_6O_{24}$ solid-state electrolyte at various temperatures. Insert is a plot of logσ vs logω_p

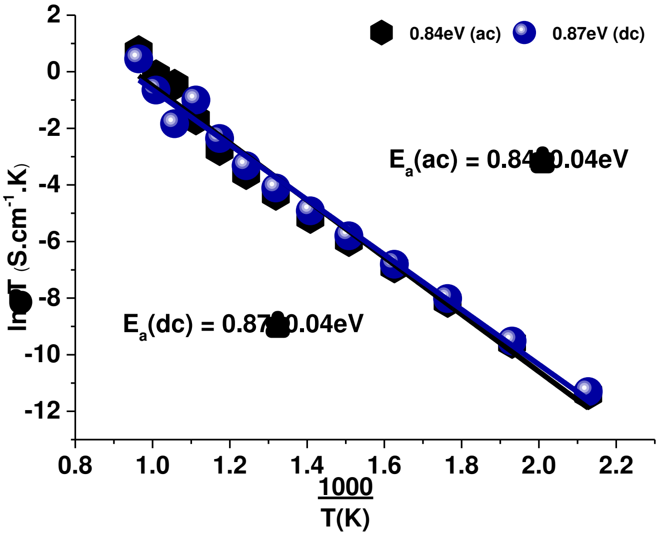

Figure 9. Comparison of dc-conductivity extracted from the low-frequency plateau with ac-conductivity of $MgZr_4P_6O_{24}$ solid-state electrolyte calculated using Arrhenius equation.

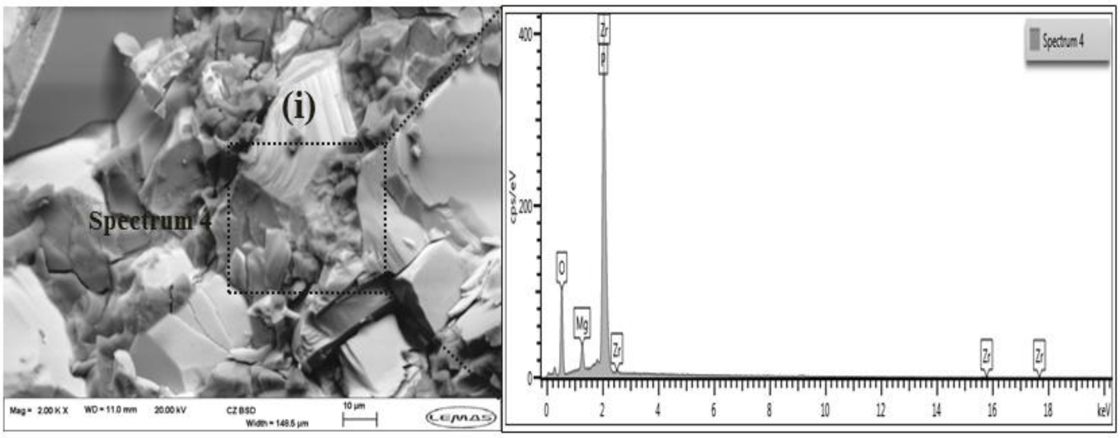

Figure 10. SEM micrographs fracture surfaces of $MgZr_4P_6O_{24}$ ceramic pellet sintered at 1300ºC and annealed for 24 h, showing its corresponding EDS spectrum 8(i)

Table 5. Average elemental composition of the EDS spectrum from fracture surface $MgZr_4P_6O_{24}$ ceramic pellet sintered at 1300°C.

Element	Atomic Fraction (%)	Atomic Ratio
Mg	2.83	1.00
Zr	11.68	4.13
P	16.53	5.84
O	68.96	24.37
Total	100.00	

Table 6. Measured open circuit voltage of the sensor at different Mg concentrations.

wt.% Mg	**N_{Mg}**	**N_{Al}**	**X_{Mg}**	**LogX_{Mg}**	**E/V**
0.005	0.0002	3.7063	5.55E-05	-4.2557	1.90
0.05	0.0021	3.7046	5.55E-04	-3.2557	2.05
0.5	0.0206	3.6879	5.55E-03	-2.2560	2.15
1.0	0.0411	3.6694	1.11E-02	-1.9552	2.19
1.5	0.0617	3.6509	1.66-02	-1.7793	2.23

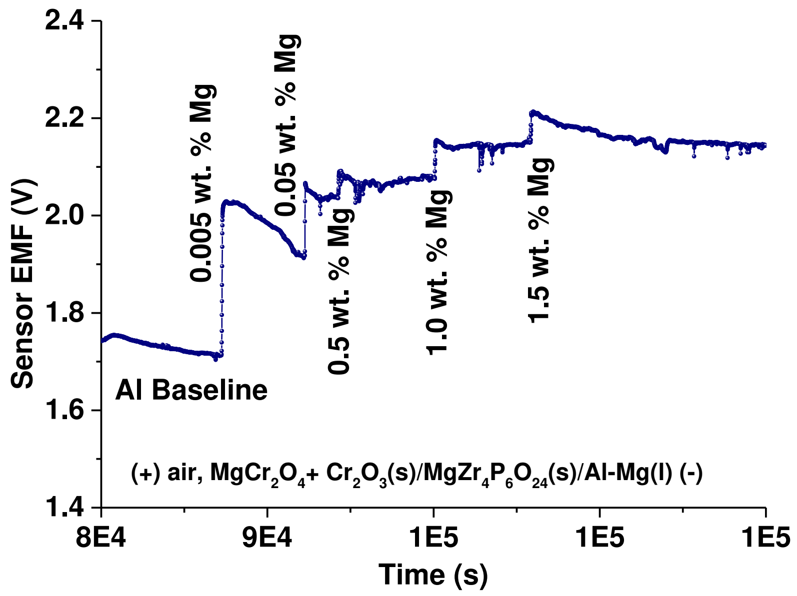

Figure 11(a). Response of solid-state Mg-sensor in molten Al as a function of time after successive addition of Mg.

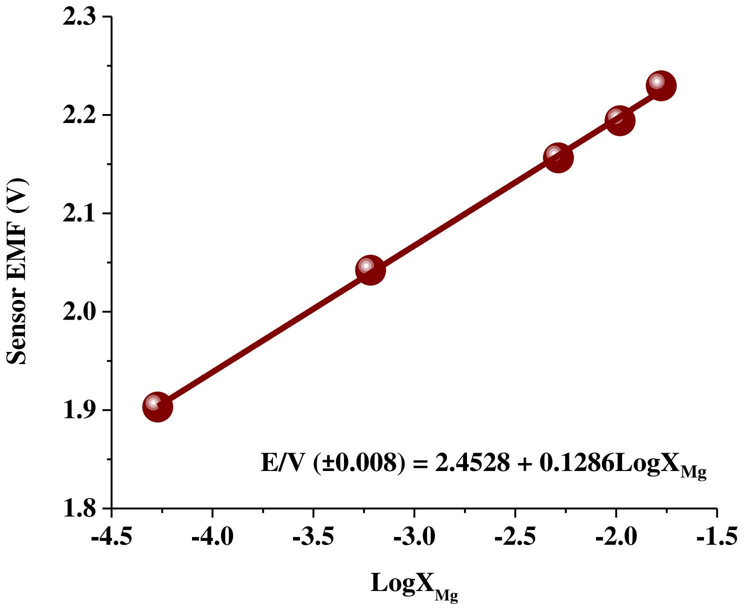

Figure 11(b). Sensor voltage variation of solid-state Mg-sensor in molten Al.

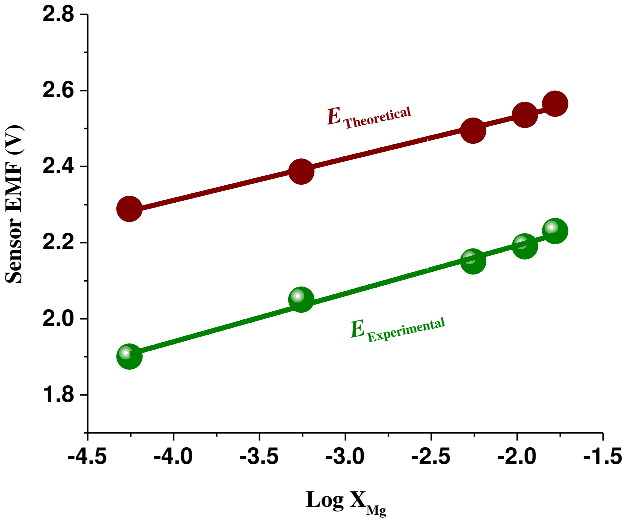

Figure 12. Comparison of the measured voltage of the sensor with the theoretical emf.

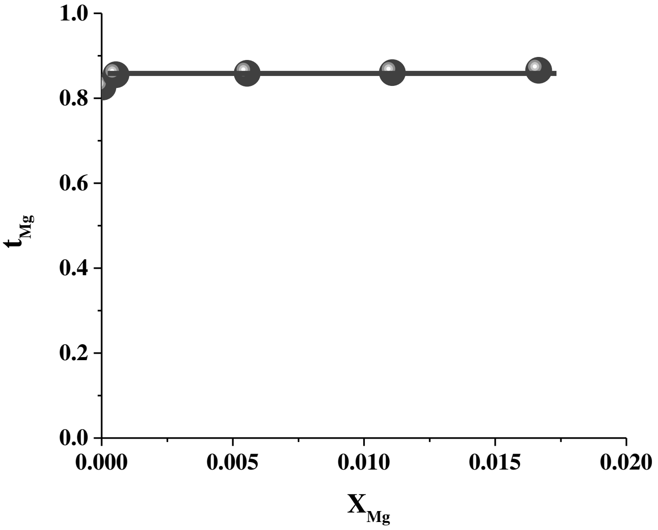

Figure 13. Variation of the average transport number of Mg^{2+}-cations in $MgZr_4P_6O_{24}$ at 700°C.